# Interfacial Dzyaloshinskii-Moriya interaction sign in Ir/$Co_2FeAl$ systems investigated by Brillouin light scattering

M. Belmeguenai,[1,*] M. S. Gabor,[2,†] Y. Roussigné,[1] T. Petrisor Jr.,[2] R. B. Mos,[2] A. Stashkevich,[1] S. M. Chérif,[1] and C. Tiusan[2,3]

[1]*LSPM, CNRS-Université Paris 13, Sorbonne Paris Cité, 99 avenue Jean-Baptiste Clément, F-93430 Villetaneuse, France*

[2]*Center for Superconductivity, Spintronics, and Surface Science, Technical University of Cluj-Napoca, Memorandumului Street, No. 28, RO-400114 Cluj-Napoca, Romania*

[3]*Institut Jean Lamour, CNRS, Université de Nancy, BP 70239, F-54506 Vandœuvre, France*

(Received 20 December 2016; revised manuscript received 5 May 2017; published 22 February 2018)

$Co_2FeAl$ (CFA) ultrathin films, of various thicknesses ($0.9\ \text{nm} \leqslant t_{CFA} \leqslant 1.8\ \text{nm}$), have been grown by sputtering on Si substrates, using Ir as a buffer layer. The magnetic properties of these structures have been studied by vibrating sample magnetometry (VSM), miscrostrip ferromagnetic resonance (MS-FMR), and Brillouin light scattering (BLS) in the Damon-Eshbach geometry. VSM characterizations show that films are mostly in-plane magnetized and the saturating field perpendicular to the film plane increases with decreasing CFA thickness suggesting the existence of a perpendicular interface anisotropy. The presence of a magnetic dead layer of 0.44 nm has been detected by VSM. The MS-FMR with the magnetic field applied perpendicularly to the film plane has been used to determine the gyromagnetic factor. The BLS measurements reveal a pronounced nonreciprocal spin wave propagation, due to the interfacial Dzyaloshinskii-Moriya interaction (DMI) induced by the Ir interface with CFA, which increases with decreasing CFA thickness. The DMI sign has been found to be the same (negative) as that of Pt/Co, in contrast to the *ab initio* calculation on Ir/Co, where it is found to be positive. The thickness dependence of the effective DMI constant shows the existence of two regimes similarly to that of the perpendicular anisotropy constant. The surface DMI constant $D_s$ was estimated to be $-0.37\ \text{pJ/m}$ for the thickest samples, where a linear thickness dependence of the effective DMI constant has been observed.

DOI: 10.1103/PhysRevB.97.054425

## I. INTRODUCTION

The exchange interaction between electrons arises from the Coulomb interaction and is responsible for the microscopic magnetic behavior. This interaction might contain symmetric and asymmetric terms. The symmetric term, imposing collinear configurations in magnetic structures, is commonly known as the Heisenberg [1] interaction. The asymmetric exchange is referred to as the Dzyaloshinskii-Moriya interaction (DMI). For the latter, Dzyaloshinskii [2] predicted, purely on grounds of symmetry, that the combination of low symmetry and spin-orbit couplings gives rise to asymmetric exchange interactions. Moriya found a microscopic mechanism which leads to such term in systems with spin-orbit coupling [3].

The DMI, which favors canted neighboring spins leading to various magnetization structures at the nanoscale such as helices [4] and skyrmions [5–7], can thus be induced by a lack of inversion symmetry and a strong spin-orbit coupling. Both these requirements are met in heavy metal/ferromagnet (HM/FM) heterostructures, giving rise to the so called interfacial DMI. High values of the DMI constants can be of great interest for chiral domain wall (DW) engineering including stabilization of Néel-type fast skyrmions for the instrumental implementation of the race-track memory. At the same time, the antisymmetric nature of the DMI excludes its doubling in a FM layer sandwiched between two identical HM films since the two contributions are mutually canceled. However, the situation can be radically changed in an asymmetric configuration if the upper and the lower HM films are characterized by DMI constants with opposite signs.

The DMI is usually characterized by its effective ($D_{\text{eff}}$) or surface ($D_s$) constants [8]. It is thus interesting for both applications and fundamental research to determine precisely the sign and the value of the DMI constant. Several experimental [9–12] and theoretical studies [13,14], largely based on how this interaction alters the properties of the DW, were performed recently. However, the experimental evaluation of $D_{\text{eff}}$ using the above mentioned techniques is at best indirect and based on strong assumptions about the dynamics and the magnetization configuration of the DW. Moreover, any numerical estimation is to be checked experimentally: sometimes, discrepancies especially in the DMI sign arise leading to unsuitable sample design [15]. Indeed, recent experiments on asymmetric DW propagation [16,17] as well as *ab initio* predictions pointed to opposite DMI signs for Ir/Co and Pt/Co [18]. Chen *et al.* confirmed this sign difference by visualizing the extent of DW chirality in perpendicularly magnetized $[Co/Ni]_n$ multilayers in contact with Pt and Ir [19]. For the above cited studies, the complex structures involving both Ir and Pt or different ferromagnets at the interfaces with Pt and Ir complicate the DMI evaluation for each interface and their comparison. For an unambiguous determination of the DMI sign, Kim *et al.* [20] investigated experimentally the thickness dependence of

*belmeguenai.mohamed@univ-paris13.fr
†mihai.gabor@phys.utcluj.ro

 

the DMI in Ir/Co/$AlO_x$ by means of Brillouin light scattering (BLS) and observed that the Pt/Co and Ir/Co interfaces have the same DMI sign. It should be emphasized that this BLS technique relying on the direct measurement of the spin wave propagation nonreciprocity is considered to be the most reliable in such studies. Thus Kim *et al.* concluded that the DMI energy is quite sensitive to the details of the multilayer structures. Therefore, attention should be paid to the whole stack when making conclusions about the sign and strength of the DMI constant. This discrepancy of DMI sign induced by Ir is summarized in Table 3 of Ref. [21], where DMI signs measured for similar samples by various methods and by different groups are presented. It raises a debate about the reliability of the *ab initio* calculations and DW observations in determining the sign of the DMI, which could even be misguiding. For example, in Ref. [15], authors, on the basis of these *ab initio* predictions, used asymmetric Ir/Co/Pt multilayers for increasing the effective DMI strength. Therefore, a direct and a precise experimental measurement of the DMI sign and magnitude is of outmost importance. Moreover, $Co_2FeAl$ is one of the most prominent Co-based Heusler alloys [22] due to its relatively high spin polarization and low magnetic damping parameter [23]. Consequently, in this work we use vibrating sample magnetometry (VSM) and microstrip ferromagnetic resonance combined with BLS to measure the magnetization at saturation and the gyromagnetic factor of Ir/$Co_2FeAl$ systems. This allows for a precise analysis of the $Co_2FeAl$ thickness dependence of the DMI constants in Ir/$Co_2FeAl$ ultrathin heterostructures. Our main purpose is to address the DMI in such as-grown complex Heusler alloys, considered as a potential candidates for application in spintronics. Indeed, since their structure and atomic disorder are both annealing and thickness dependent, they give the opportunity to investigate the DMI dependence with the atomic distribution at interfaces. This latter aspect is very interesting and reveals nonregular behavior which can trigger consideration on theories and models to explain the observed trends. The effect of the annealing temperature on the DMI in a $Co_2FeAl$ ultrathin film will be addressed in a forthcoming paper. Moreover, we show that the effective constant demonstrates the pattern of a behavior similar to that reported by Kim *et al.* for Ir/Co [20,21]: it is thickness and interface dependent while its sign is identical to that induced by Pt (in Pt/Co systems).

## II. SAMPLES AND EXPERIMENTAL TECHNIQUES

$Co_2FeAl$ (CFA) thin films were grown at room temperature on a Si substrate covered with a 100 nm thick thermally oxidized $SiO_2$ layer using a magnetron sputtering system with a base pressure lower than $2\times10^{-8}$ Torr. Prior to the deposition of the CFA film, a 2 nm thick Ta seed layer and a 4 nm thick Ir layer were deposited on the substrate. Next, CFA films, with variable thicknesses ($0.9\,\text{nm} \leqslant t_{\text{CFA}} \leqslant 1.8\,\text{nm}$), were deposited at room temperature by dc sputtering under an argon pressure of 1 mTorr, at a rate of 0.1 nm/s. Finally, in order to protect the structure from air exposure, a 2 nm thick Ti film was deposited on top of the CFA layer. In these heterostructures, the Ir layer induces DMI in the CFA ultrathin layers, while Ti is only used to protect CFA from oxidation. It is expected to induce no DMI contribution, since it is not a heavy metal.

The crystal structure of the films was studied by x-ray diffraction (XRD) using a four-circle diffractometer. VSM has been used to measure hysteresis loops with the magnetic field applied perpendicular or parallel to the films plane and to determine static magnetic parameters. Microstrip line ferromagnetic resonance (MS-FMR) [23] has been employed here for determining the gyromagnetic factor for the thickest samples ($t_{\text{CFA}} \geqslant 1.2\,\text{nm}$), for which a MS-FMR signal has been detected.

In the BLS setup, the spin waves (SWs), of a wave number ($k_{\text{sw}}$) in the range $0-20\,\mu\text{m}^{-1}$ [depending on the incidence angle $\theta_{\text{inc}}$ : $k_{\text{sw}} = \frac{4\pi}{\lambda}\sin(\theta_{\text{inc}})$ in backscattering configuration], are probed by illuminating the sample with a laser having a wavelength $\lambda = 532\,\text{nm}$. The magnetic field was applied perpendicular to the incidence plane, which allows for probing spin waves propagating along the in-plane direction perpendicular to the applied field, i.e., in the Damon-Eshbach (DE) geometry where the DMI effect on the SW propagation nonreciprocity is maximal [24]. For each angle of incidence, the spectra were obtained after sufficiently counting photons to have well-defined spectra where the line position can be determined with accuracy better than 0.2 GHz. The Stokes (S; negative frequency shift relative to the incident light as a magnon was created) and anti-Stokes (AS; positive frequency shift relative to the incident light as a magnon was absorbed) frequencies, detected simultaneously, were then obtained from Lorentzian fits to the BLS spectra. For identical interfaces, S and AS lines should have the same frequency. In the presence of the DMI on one interface, the frequency difference between these two counterpropagating SWs exists and increases with $k_{\text{sw}}$. Therefore, the DMI constants are determined from $k_{\text{sw}}$ dependence of the frequency difference between S and AS lines.

For the analysis of the BLS measurements, the DE mode dispersion [25,26], taking into account the DMI contribution, is given by the equation

$$F = F_0 + F_{\text{DMI}} = \mu_0\frac{\gamma}{2\pi}\sqrt{\left[H + Jk_{\text{sw}}^2 + P(k_{\text{sw}}t_{\text{FM}})M_s\right]\left[H + Jk_{\text{sw}}^2 - P(k_{\text{sw}}t_{\text{FM}})M_s + M_{\text{eff}}\right]} \pm \frac{\gamma}{\pi M_s}D_{\text{eff}}k_{\text{sw}}. \quad (1)$$

Here $H$ is the in-plane applied magnetic field, $t_{\text{FM}}$ is the ferromagnetic layer thickness, $\mu_0$ is the permeability of vacuum, and $A_{\text{ex}}$, in $J = \frac{2A_{\text{ex}}}{\mu_0 M_s}$, is the exchange stiffness constant. The coefficient $P(k_{\text{sw}}t_{\text{FM}}) = 1 - \frac{1-\exp(-k_{\text{sw}}t_{\text{FM}})}{k_{\text{sw}}t_{\text{FM}}}$ describes dipolar interactions. It is reduced, in thin films ($k_{\text{sw}}t_{\text{FM}} \ll 1$), to a simple $P(k_{\text{sw}}t_{\text{FM}}) = \frac{k_{\text{sw}}t_{\text{FM}}}{2}$, which makes this term linear in $k_{\text{sw}}t_{\text{FM}}$. It should be noted that in our case $k_{\text{sw}}t_{\text{FM}} \approx 0.02$.

We define the interfacial DMI constant as $D_s = D_{\text{eff}} \times t_{\text{FM}}$. From this, the frequency difference can be inferred to be

$$\Delta F = F_{\text{S}} - F_{\text{AS}} = \frac{2\gamma}{\pi M_s}D_{\text{eff}}k_{\text{sw}} = \frac{2\gamma}{\pi M_s}\frac{D_s}{t_{\text{FM}}}k_{\text{sw}}. \quad (2)$$

According to Eq. (1), the dispersion splits into two branches corresponding to the frequency of the Stokes $F_{\text{S}}$ and the

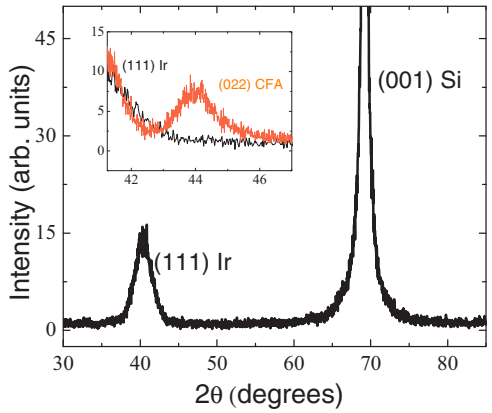


FIG. 1. $2\theta/\omega$ (out-of-plane) x-ray diffraction pattern measured for the sample with $t_{CFA} = 1$ nm. The inset shows a detail of the $2\theta/\omega$ x-ray diffraction patterns of both the 1 nm and 6 nm thick CFA layer samples.

anti-Stokes $F_{AS}$ lines. Each frequency results from two contributions. (i) The major one (being field dependent) takes into account the dipole-dipole interactions linear in $k_{sw}$ (in ultrathin films such as ours) and a quadratic in $k_{sw}$ contribution of the conventional isotropic exchange. (ii) The DMI contribution (linear in $k_{sw}$) is described by a smaller addition whose sign depends on whether one is interested in the S or AS frequency shift. Importantly, if $F_S$ is lower than $F_{AS}$, then the resulting DMI constant is negative for a positive applied magnetic field.

## III. RESULTS AND DISCUSSION

### A. Structural properties

Measurements presented here were performed at room temperature. Figure 1 shows a $2\theta/\omega$ (out-of-plane) x-ray diffraction pattern measured for the sample with $t_{CFA} = 1$ nm. One can observe that, except for the peak corresponding to the Si substrate, the pattern shows only the (111) Ir peak. This suggests that the Ir layer has a strong (111) out-of-plane texture. The absence of a diffraction peak from the Ta layer indicates, as expected, that the film is in an amorphous state. The same result might be valid for the CFA layer, but it is unlikely, having in view that the lower Ir layer has a strong (111) texture. In order to test this, we have grown a sample with a much thicker CFA layer of 6 nm. The inset of Fig. 1 shows a detail of the $2\theta/\omega$ x-ray diffraction patterns of both the 1 nm and the 6 nm thick CFA layers samples. A diffraction maximum is clearly visible for the 6 nm thick CFA sample at a $2\theta$ around 44°, which can be attributed to the (022) CFA reflection. The absence of the (022) diffraction peak for the 1 nm thick CFA films is a consequence of the ultralow thickness of the film thus corroborating the relatively low atomic scattering factors of the CFA constituents. No other additional diffraction peaks were observed for the 6 nm thick CFA sample as compared to the 1nm thick CFA samples. This indicates that the CFA films show a (022) out-of-plane texture. Furthermore, $\varphi$-scan measurements (not shown here) showed that both Ir and CFA have no in-plane texturing but in-plane isotropic distribution of the crystallites.

### B. Magnetic properties and gyromagnetic ratio determinations

Figures 2(a) and 2(b) show the in-plane and the out-of-plane hysteresis loops measured for the sample with a CFA thickness of 1.8 nm. The out-of-plane hysteresis loop indicates a continuous rotation of the magnetization towards the perpendicular direction as the magnetic field is increased. This indicates that the sample possesses an in-plane anisotropy easy axis. A weak uniaxial anisotropy was observed in the plane, as indicated by the different shape of the hysteresis loops measured in-plane [Fig. 2(a)]. The presence of the small uniaxial in-plane anisotropy is not unusual for sputtered films and it is maybe due to a residual magnetic field present during growth. It is to be mentioned that the other samples show a similar behavior due to the weak in-plane anisotropy (not exceeding 50 Oe according to FMR investigations), except for the sample with a CFA thickness of 0.9 nm, whose in-plane and out-of-plane hysteresis loops are shown in Figs. 2(c) and 2(d). As we will see below, this sample is at the limit between in-plane and perpendicular magnetic anisotropy and most likely it shows a complex domain structure rendering the null remanence magnetization. We think that this sample could present a weak in-plane anisotropy as the other films. Although the in-plane anisotropy for the in-plane magnetized films has been detected mainly by FMR measurements, it was not possible to use FMR for the 0.9 nm thick film due to the weak signal and the high required in-plane saturation field. Moreover, the in-plane applied fields used during BLS measurements exceed a 4 kOe which is significantly higher than the small in-plane anisotropy present in all samples. We should mention that the magnetization in Fig. 2 was evaluated by considering the nominal CFA thickness, which explains the difference of the magnetization at saturation between the 1.8 nm and the 0.9 nm thick CFA films since the magnetic dead layer is not taken into account.

Figure 3(a) depicts the CFA thickness dependence of the saturation magnetic moment per unit area, which is used to determine the magnetization at saturation ($M_s$) and the magnetic dead layer thickness ($t_d$): the slope of the linear fit of the data gives $M_s$, while the horizontal axis intercept gives $t_d$. The thickness of the magnetic dead layer and magnetization at saturation are found to be 0.44 nm and $1035 \pm 55$ emu/cm$^3$ (error bar less than 6%). The magnetic dead layer is most probably due to intermixing at the Ir/CFA interface, since the deposition of a heavy metal onto a ferromagnet (or vice versa) is usually accompanied by such mixing effects. Therefore, the magnetic dead layer should be taken into account for the CFA effective thickness to be used when determining the effective anisotropy and DMI constants. Even though a dead layer at the bottom interface exists, this does not completely cancel the DMI interaction, as will be experimentally shown below. The increase of $M_s$ for the Ir/CFA system, compared to that of MgO/CFA/MgO ($M_s \sim 850 \pm 50$ emu/cm$^3$) [27], is most likely due to the proximity-induced magnetization in Ir. This corresponds to a change in the film magnetization of 22%, which is slightly higher than the reported value (19%) in Ir/Co/Ni/Co [28] and Ir/Co [20] systems.

The $g$ value, which determines the gyromagnetic factor and therefore the precision of the evaluation of the DMI constant, is precisely accessible by the MS-FMR technique, through the study of the frequency variation versus the magnetic field

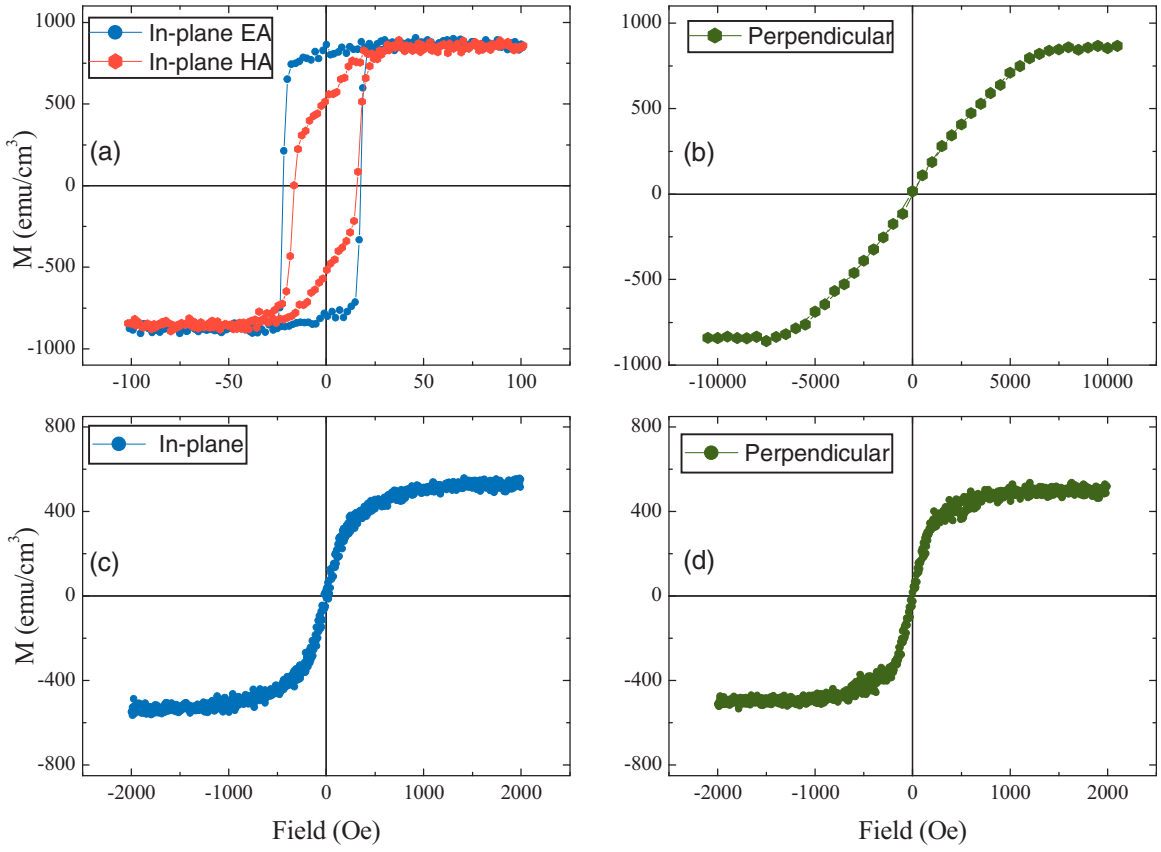


FIG. 2. (a) In-plane and (b) out-of-plane hysteresis loops measured for the sample with a CFA thickness of 1.8 nm. (c) In-plane and (d) out-of-plane hysteresis loops measured for the sample with a CFA thickness of 0.9 nm. The magnetization was evaluated by considering the nominal CFA thickness.

applied perpendicularly to the film plane. A typical MS-FMR perpendicular field dependence of the resonance frequency ($F_\perp$) is shown in Fig. 3(b). The linear variation of $F_\perp$ as a function of the magnetic field is in agreement with the expected theoretical dependence given by $F_\perp = (\frac{\gamma}{2\pi})(H - 4\pi M_{\text{eff}})$, where $(\gamma/2\pi) = g \times 1.397 \times 10^6$ Hz/Oe is the gyromagnetic factor and $M_{\text{eff}}$ is the effective magnetization [23]. The derived value of $g = 2.04$ ($\gamma/2\pi = 29.2$ GHz/T) is in excellent agreement with the value determined in our previous papers [23,29] for relatively thick CFA films. Since this value does not present a significant variation versus the CFA thickness [at least for the thickest CFA films ($t_{\text{CFA}} \geqslant 1.2$ nm), for which a MS-FMR signal has been detected], it will be used for all samples studied here.

To quantify the magnitude of the perpendicular magnetic anisotropy of our films, we determined the effective

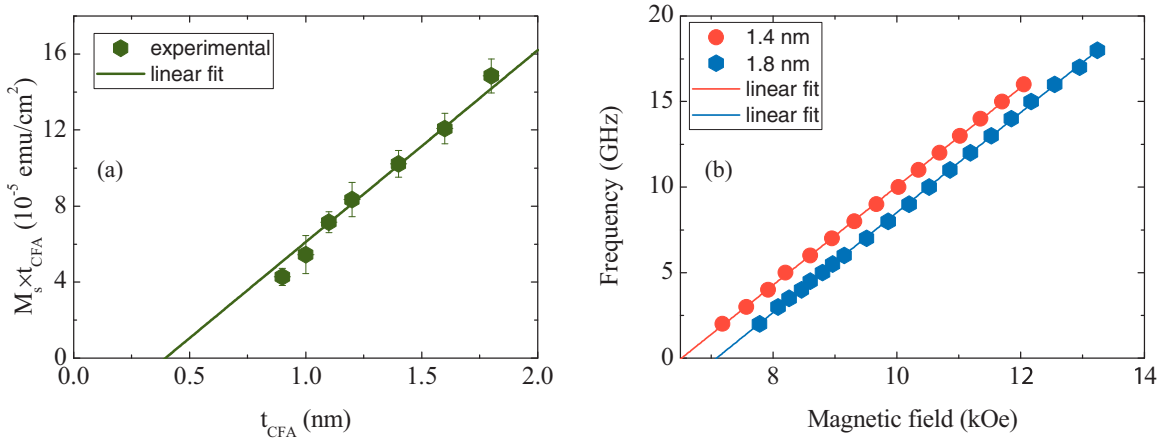


FIG. 3. (a) The thickness dependence of the saturation magnetic moment per unit area. (b) MS-FMR perpendicular applied magnetic field dependence of the resonance frequency measured for samples with CFA thicknesses of 1.4 nm and 1.8 nm, respectively.

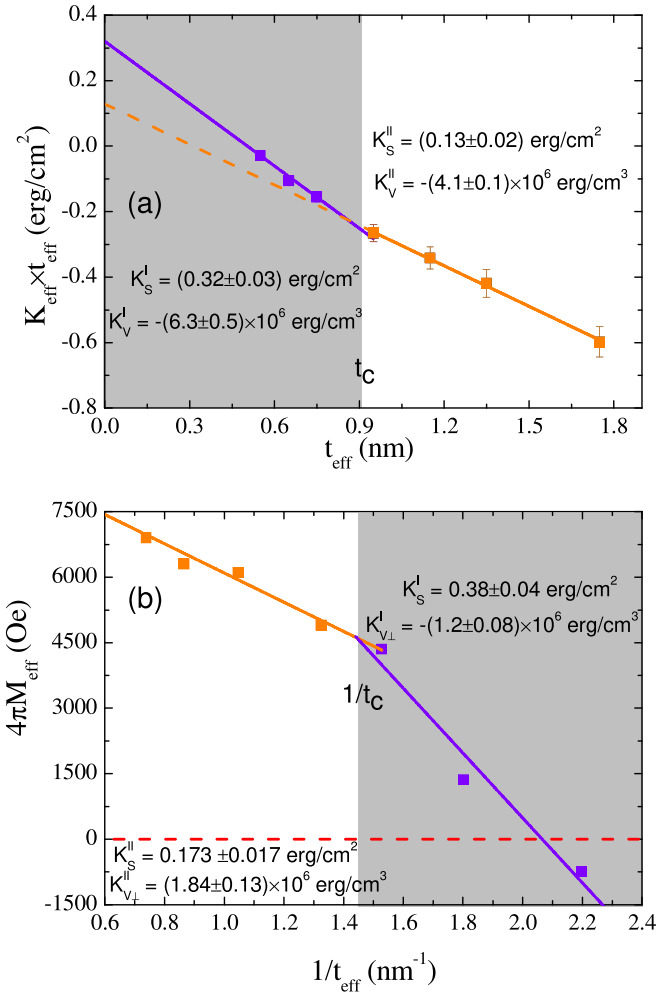


FIG. 4. (a) $K_{\rm eff} \times t_{\rm eff}$ versus the effective CFA thickness deduced from perpendicular applied magnetic field hysteresis loops. (b) Thickness dependence of the effective magnetization ($4\pi M_{\rm eff}$) extracted from the fit of BLS ($t_{\rm CFA} < 1.2$ nm) and MS-FMR ($t_{\rm CFA} \geqslant 1.2$ nm) measurements. Symbols refer to experimental data while solid lines are the linear fits corresponding to the two regimes. For a direct comparison between the anisotropy constants indicated in panels (a) and (b), note that $K_v^i = K_{v\perp}^i - 2\pi M_s^2$, where the superscript $i$ refers to regime I or II.

perpendicular magnetic anisotropy constant $K_{\rm eff}$ from the saturation field ($H_s$) in the hard plane, using the relation $K_{\rm eff} = -M_s H_s/2$. The $H_s$ value was determined from the hysteresis loops perpendicular to the film plane [see Fig. 2(b)]. Phenomenologically, the $K_{\rm eff}$ dependence on the thickness can be separated into a volume ($K_v$) and a surface contribution ($K_s$) as $K_{\rm eff} \times t_{\rm eff} = K_v \times t_{\rm eff} + K_s$, where $t_{\rm eff} = t_{\rm CFA} - t_d$ is the CFA effective thickness [30,31]. As depicted in Fig. 4(a), the $K_{\rm eff} \times t_{\rm eff}$ does not show a single linear dependence on the $t_{\rm eff}$ for the whole thickness range. Instead, there are two regions separated by a critical thickness $t_c$, each with its own linear dependence, characterized by different slopes. Several explanations can be given to the deviation from the single linear behavior of the perpendicular effective anisotropy versus the CFA effective thickness [30] and therefore to the existence of a second regime of higher effective anisotropy, as shown in Fig. 4. The four most important mechanisms will be discussed separately and will be used to analyze our experimental data. First, a possible coherent-incoherent growth transition, with the accompanying changes in the magnetoelastic anisotropy contributions, can lead to this two-regime behavior. This is commonly observed in thin-film systems in which there is an elastic strain relaxation above a certain critical thickness [30–32]. In the case of our samples, since Ir and CFA grow with a (111) and (011) out-of-plane texture and having in view the lattice parameters of the two films, we expect that at the first stages of the growth, CFA is to be subdued to an in-plane compressive stress which at least partially relaxes through the formation of misfit dislocations as thickness is increased.

In order to analyze the results and according to the model from [30,31], we will consider two regimes: below (regime I) and above (regime II) the critical thickness, in which $K_v$ and $K_s$ are given by

$$\begin{aligned} K_v^I &= -2\pi M_s^2 + K_{\rm mc} + K_{{\rm me},v}, \\ K_s^I &= K_N, \end{aligned} \quad \text{in regime I,} \tag{3}$$

$$\begin{aligned} K_v^{II} &= -2\pi M_s^2 + K_{\rm mc}, \\ K_s^{II} &= K_N + K_{{\rm me},s}, \end{aligned} \quad \text{in regime II.} \tag{4}$$

Here $K_{\rm mc}$ is the magnetocrystalline anisotropy, $K_{{\rm me},v}$ and $K_{{\rm me},s}$ are the volume and the interface magnetoelastic anisotropy constants, $2\pi M_s^2$ is the shape anisotropy contribution, and $K_N$ is the Néel-type perpendicular interface anisotropy constant induced by the broken symmetry at the interfaces. According to this model, in region I, the influence of the misfit strain appears as a volume contribution (characterized by $K_{{\rm me},v}$) to the anisotropy. Although it is bulk related, this misfit leads to an apparent interface contribution in regime II [30,31] (characterized by $K_{{\rm me},s}$).

The linear fit of measurements in Fig. 4 allows us to determine constants for both regimes from the slope and the intercept with the vertical axis, respectively. Then, by using Eqs. (3) and (4), contributions of the magnetocrystalline, magnetoelastic, and Néel-type interface anisotropies to the surface and the volume perpendicular anisotropies have been separately estimated: $K_{\rm mc} = (2.6 \pm 0.1) \times 10^6$ ergs/cm$^3$, $K_{{\rm me},v} = -(2.2 \pm 0.6) \times 10^6$ ergs/cm$^3$, $K_{{\rm me},s} = -(0.18 \pm 0.05)$ ergs/cm$^2$, and $K_N = (0.32 \pm 0.03)$ ergs/cm$^2$. The magnetoelastic anisotropy is negative reinforcing the in-plane easy axis. The Néel-type surface interface anisotropy, reinforcing the perpendicular easy axis, can be mainly attributed to the Ir/CFA interface [31]. Both volume and surface magnetoelastic anisotropies are negative and thus reinforce the in-plane easy axis. This is coherent with the fact that CFA films are in-plane compressed and with the positive magnetostriction coefficient of CFA [33]. In order to furthermore confirm the observed trend of the out-of-plane magnetic anisotropy of our films, we have determined the effective magnetization ($4\pi M_{\rm eff} = 4\pi M_s - \frac{2K_\perp}{M_s}$, where $K_\perp$ is the perpendicular anisotropy constant) using both BLS and MS-FMR techniques. BLS is used for the thinner samples (0.9 nm $\leqslant t_{\rm CFA} \leqslant$ 1.1 nm), where the MS-FMR signal was not sufficient to follow the field dependence of the precession frequency. The extracted values are shown in Fig. 4(b), as a function of $1/t_{\rm eff}$. Depending on $t_{\rm CFA}$,

two different regimes, separated by a critical thickness $t_c$ (nominal CFA thickness around 1 nm) can be distinguished. For both regimes, $M_{\text{eff}}$ decreases linearly with $1/t_{\text{eff}}$ but with different slopes: the slope is higher for $t < t_c$. The linear fit of the measurements of Fig. 4(b) allows determining the perpendicular surface and volume anisotropy constants for both regimes from the slope and the intercept with the vertical axis, respectively, since the perpendicular anisotropy constant $K_\perp$ obeys the relation $K_\perp = K_{v\perp} + \frac{K_s}{t}$. In this formula, $K_s$ accounts for the two interface contributions induced by Ir and Ti. Then, by using Eqs. (3) and (4), the MS-FMR anisotropy constants [$K_{\text{mc}} = (1.84 \pm 0.13) \times 10^6\,\text{ergs/cm}^3$, $K_{\text{me},v} = -(3.04 \pm 0.21) \times 10^6\,\text{ergs/cm}^3$, $K_{\text{me},s} = -0.21 \pm 0.057\,\text{ergs/cm}^2$, and $K_N = 0.384 \pm 0.04\,\text{ergs/cm}^2$] are in good agreement with the ones deduced from the static measurements.

Another possible way to explain the two-regime behavior is the roughness in the thinner films. Such roughness creates in-plane demagnetizing fields at edges of terraces reducing the shape anisotropy and therefore favors a perpendicular magnetization: the effective magnetization $4\pi M_{\text{eff}}$ is modified into $4\pi M_{\text{eff}} = (4\pi - N_x - N_y)M_s - \frac{2K_\perp}{M_s}$, where $N_x, N_y$ are the in-plane demagnetizing factors. In the case of a perfectly flat film, $N_x = N_y = 0$, $N_z = 4\pi$, while edges of discontinuities yield an increase of $N_x$ and $N_y$. The influence of the roughness has been calculated in the frame of the dipolar approximation by Szymczak *et al.* [34]: $(4\pi - N_x - N_y) = 4\pi - 3\pi(\sigma/t)(1 - f)$. In this expression, $\sigma$, which is a statistical parameter characterizing the roughness, is the average deviation from the reference plane and $f$ is a tabulated factor depending on the geometric parameters. According to this model, the surface anisotropy constant ($K_r$) due to the roughness is given by

$$K_r = \tfrac{3}{2}\pi M_s^2 \sigma (1 - f). \tag{5}$$

In the regime of thinner films, the surface anisotropy constant is thus $K_s^I = K_s^{II} + K_r$. By using $K_s^I$ and $K_s^{II}$ values, obtained from the linear fit of the experimental data shown in Fig. 4, we determine $\sigma \sim 0.6\,\text{nm}$ and $f \sim 0.2$ (Fig. 4 in Ref. [34]). This very high roughness value is not reasonable, since the usual measured one in such samples is about 0.3 nm. Moreover, as the effective CFA thickness is comparable to $2\sigma$ (terrace height) in the case of thinner films, this roughness value implies the occurrence of discontinuities in the thinner films. Furthermore, discontinuities in the CFA films yield a lower effective magnetic/nonmagnetic interface area. This leads thus to a lower interface contribution and a correspondingly lower total anisotropy. Consequently, the effective magnetization should increase. Therefore, to take the discontinuity effect on interface anisotropy into account, one should consider a roughness larger than the above estimation $\sigma > 0.6\,\text{nm}$. This yields a terrace height superior to 1.2 nm which is not meaningful because the thinnest film thickness is inferior to this value.

Finally, interdiffusion and mixing might occur at interfaces during the deposition of layers. It introduces thus randomness in the magnetic pair bonds, which obviously reduces the interface anisotropy [30]. This latter mechanism is incompatible with the experimental results shown in Fig. 4, where a higher effective anisotropy is observed for thinner films: below $t_c$.

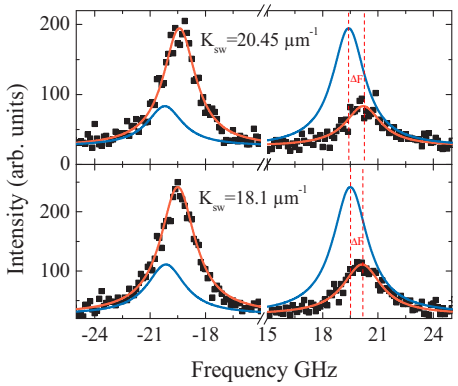


FIG. 5. BLS spectra measured for 1.4 nm thick CFA film at a 4 kOe in-plane applied magnetic field and at two characteristic light incidence angles corresponding to $k_{\text{sw}} = 18.1$ and $20.45\,\mu\text{m}^{-1}$. Symbols refer to experimental data and solid lines are the Lorentzian fits. Fits corresponding to negative applied fields (blue lines) are presented for clarity and direct comparison of the Stokes and the anti-Stokes frequencies.

The consistence of the two first models with our experimental results will be further discussed below after presenting the determination of the DMI constant.

### C. DMI investigation and discussion

Figure 5 shows the typical BLS spectra for the 1.4 nm thick sample for $k_{\text{sw}} = 18.1\,\mu\text{m}^{-1}$ ($\theta_{\text{inc}} = 50°$) and $20.45\,\mu\text{m}^{-1}$ ($\theta_{\text{inc}} = 60°$). It reveals the existence of both S and AS spectral lines. Besides the usual intensity asymmetry of these lines due to the coupling mechanism between the light and SWs, a pronounced difference between the frequencies of the S and AS lines ($\Delta F = F_{\text{S}} - F_{\text{AS}}$) is revealed by the BLS spectra. This frequency mismatch, more significant for higher values of $k_{\text{sw}}$, is due to the interfacial DMI as demonstrated previously [8,24,26]. Since the inverse proportionality to the ferromagnetic layer thickness is usually a signature of an interface effect, the behavior of $\Delta F$ versus $1/t_{\text{eff}}$ is presented in the inset of Fig. 6(a) for $k_{\text{sw}} = 20.45\,\mu\text{m}^{-1}$ ($\theta_{\text{inc}} = 60°$). It can be observed that $\Delta F$ increases with $1/t_{\text{eff}}$ and approaches zero when $t_{\text{CFA}}$ tends to infinity, confirming the interfacial origin of the DMI. Figure 6(a) shows the $k_{\text{sw}}$ dependence of $\Delta F$ for CFA thin films of various thicknesses, where a clear linear behavior can be observed. From the slopes of the $k_{\text{sw}}$ dependences of $\Delta F$, the effective DMI constants have been extracted using Eq. (2) with $\gamma/(2\pi) = 29.2\,\text{GHz/T}$ and $M_s = 1035\,\text{emu/cm}^3$ deduced from the fit of MS-FMR data and the VSM measurements, respectively. The evolution of the obtained values of $D_{\text{eff}}$ as a function of the inverse of the CFA film's effective thickness ($1/t_{\text{eff}}$) is shown in Fig. 6(b) where a linear behavior can be observed, as predicted theoretically. Note the deviation from the linearity, as the CFA nominal thickness approaches 1.1 nm similarly to the thickness dependence of the perpendicular anisotropy (Fig. 4). Two regimes (above and below CFA nominal thickness of 1.1 nm) with different slopes can be distinguished. By the linear fit of the data of Fig. 5(b) for $t_{\text{CoFe}} \geqslant 1.1\,\text{nm}$, $D_s$ has been found to be $-0.34\,\text{pJ/m}$. This value is significantly lower

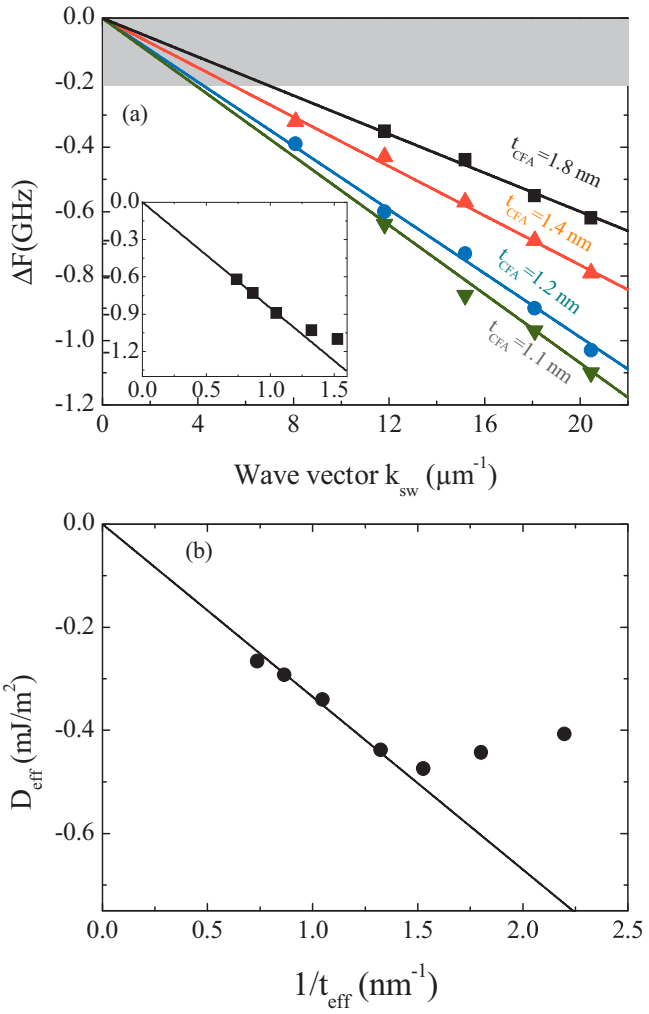


FIG. 6. (a) Wave vector ($k_{sw}$) dependence of the experimental frequency difference $\Delta F$ of CFA films of a thickness $t_{CFA}$ grown on Si substrates. Solid lines refer to a linear fit using Eq. (2) and magnetic parameters in the text. The inset of the figure shows the frequency difference $\Delta F$ of CFA films for light incidence angles corresponding to $k_{sw} = 20.45$ as a function of the inverse of the effective thickness of CFA films ($1/t_{eff}$). Symbols refer to experimental data and the straight solid line is the linear fit. (b) Thickness dependence of the effective DMI constant extracted from fits of Fig. 5(a). Solid lines refer to the linear fit.

than that of Pt/Co/$AlO_x$ systems [17] but has the same sign as Pt/Co, confirming the recent results of Kim *et al.* [20] for Ir/Co. However, it is slightly lower than the one measured for Ir/Co ($-0.8$ pJ/m) [20] most probably because authors ignored the magnetic dead layer when determining $D_s$. Moreover, CFA films (as all the Heusler alloys) are subject to some degree of chemical disorder, which strongly influences many of their physical properties and thus DMI. Thinner films (thickness below 10 nm) annealed at low temperature (below 300 °C) have the A2 structure, corresponding to a complete disorder between all atoms Co, Fe, and Al [27]. Therefore, within the CFA thickness range presented in this paper, all films have mostly the same disordered A2 structure. This may explain the smaller DMI constant in Ir/CFA compared to Ir/Co. By considering the evolution of the obtained values of $D_{eff}$ as a function of the reciprocal nominal thickness of CFA films (not shown here) the deduced value of $D_s$ ($-0.51$ pJ/m) is comparable to that of Ir/Co [20]. It is worth recalling the discrepancy of the DMI sign induced by the DMI as summarized in Table 3 of Ref. [21].We should mention that the existence of the two regimes of the thickness dependence of $D_{eff}$ has been observed for Pt/CoFe systems [35] and Pt/CoFeB [36], in contrast to Pt/Co systems [36]. Moreover, this piecewise linear behavior seems to be a characteristic of alloyed ferromagnetic films. It seems to be more significant as the number of atoms constituting the alloy increases. For example, the two regimes of the thickness dependence of $D_{eff}$ have different slopes with the same sign in the case of CoFe [35], while an inversion of the trend has been observed for CoFeB [36] and here for CFA. Although the diminution of $D_{eff}$ as the thickness decreases was directly correlated with the interface degradation in the case of Pt/CoFe [35] and Pt/CoFeB [36], this correlation is not obvious in Ir/CFA. Since slopes of the thickness dependence of $M_{eff}$ and $D_{eff}$ for ultrathin films ($t_{eff} < t_c$) have opposite signs—for $t_{eff} < t_c$, the effective surface anisotropy (surface DMI constant) is higher (lower) than that for $t_{eff} > t_c$—other mechanisms should be involved. Therefore, the existence of the two regimes can be understood through the above mentioned first and second mechanisms for the perpendicular anisotropy. In the light of the first mechanism, for the thickest CFA films ($t_{eff} > t_c$), the stress induced by growth is relaxed by dislocations at the interface. Therefore, $D_s$ and $D_{eff}$ obey the standard relation $D_{eff} = D_s/t_{eff}$, as observed in Fig. 6(b). In the regime of low thicknesses ($t_{eff} < t_c$), the CFA films are strained (compressive stress) and the interface is without dislocations. Therefore, the distance between Ir and CFA atoms at the interface changes, modifying thus the DMI constant, according to Fert *et al.* [37]. In the frame of the second approach mentioned above, CFA film discontinuities at interfaces decrease the contact surface between Ir and CFA reducing thus both the DMI and the anisotropy constant for thinner films. Finally, it is worth mentioning that Nembach *et al.* [38] demonstrated a linear proportionality between the exchange stiffness constant and DMI. Furthermore, they observed a nonlinear thickness dependence of the effective DMI constant in Pt/Py. They thus speculated that this nonlinear behavior results from an unexpected thickness dependence of the symmetric exchange interaction for this particular system. The microscopic origins of the variation of the symmetric exchange interaction with film thickness are unclear. Moreover, it is an empirical fact that both the symmetric exchange and the asymmetric exchange interactions exhibit the same nontrivial functional dependence on reciprocal thickness as acknowledged by Nembach [38]. Since it is not possible to precisely measure the exchange stiffness constant by BLS for such ultrathin CFA films, the thickness dependence of the exchange stiffness constant in our ultrathin films cannot be checked. Therefore, it is not possible to speculate about this behaviour. Consequently, this possible interpretation of the thickness dependence of the DMI cannot be verified.

Due to the lack of the precise information about the residual strain, the interface quality, and the thickness dependence of the exchange stiffness constant in our samples, it is not obvious to identify the mechanism responsible for both the decrease of

$D_{\text{eff}}$ and the increase of the surface anisotropy for the thinner CFA films. However, we strongly believe that the CFA film growth discontinuities at the interface with Ir are not compatible with thickness dependence of the effective perpendicular anisotropy and therefore, the probable responsible mechanism for both behaviors of the DMI and the effective perpendicular anisotropy is a possible coherent-incoherent transition.

## IV. CONCLUSIONS

CFA films of various thicknesses ($0.9\,\text{nm} \leqslant t_{\text{CFA}} \leqslant 1.8\,\text{nm}$) were prepared by sputtering on Ta/Ir-buffered $Si/SiO_2$ substrates. The vibrating sample magnetometry measurements revealed that the CFA films are in-plane magnetized. Ferromagnetic resonance with a microstrip line has been used to determine the gyromagnetic ratio, and Brillouin light scattering has been employed in the Damon-Eshbach geometry to investigate the spin wave nonreciprocity induced by the interfacial Dzyaloshinskii-Moriya interaction (DMI). It turned out that the DMI effective constant sign of Ir/CFA is the same as the Pt/Co and Ir/Co ones (deduced from BLS experiments), in contrast to that of Ir/Co which was found to be of opposite sign according to both the theoretical calculations and some experimental observations on such Ir/Co systems. Indeed, recent experiments on asymmetric DW propagation as well as *ab initio* predictions both point to opposite DMI signs for Co/Ir and Co/Pt.

## ACKNOWLEDGMENTS

M.B. would like to thank A. Thiaville for fruitful discussions and remarks. This work has been partially supported by the Conseil Régional, Île-de-France, through the DIM NanoK (BIDUL project). M.S.G., T.P., and R.B.M. acknowledge the financial support of UEFISCDI through PN-II-RU-TE-2014-4-1820 SPINCOD Research Grant No. 255/01.10.2015.

[1] W. Heisenberg, Z. Phys. **49**, 619 (1928).
[2] I. E. Dzyaloshinskii, Sov. Phys. JETP **5**, 1259 (1957).
[3] T. Moriya, Phys. Rev. **120**, 91 (1960).
[4] J. Kishine and A. Ovchinnikov, Solid State Phys. **66**, 1 (2015).
[5] U. K. Roszler, A. N. Bogdanov, and C. Pfleiderer, Nature (London) **442**, 797 (2006).
[6] C. Felser, Angew. Chem., Int. Ed. **52**, 1631 (2013).
[7] N. Nagaosa and Y. Tokura, Nat. Nanotechnol. **8**, 899 (2013).
[8] M. Belmeguenai, J.-P. Adam, Y. Roussigné, S. Eimer, T. Devolder, J.-V. Kim, S. M. Chérif, A. Stashkevich, and A. Thiaville, Phys. Rev. B **91**, 180405(R) (2015).
[9] J. Torrejon, J. Kim, J. Sinha, S. Mitani, M. Hayashi, M. Yamanouchi, and H. Ohno, Nat. Commun. **5**, 4655 (2014).
[10] S. Pizzini, J. Vogel, S. Rohart, L. D. Buda-Prejbeanu, E. Jué, O. Boulle, I. M. Miron, C. K. Safeer, S. Auffret, G. Gaudin, and A. Thiaville, Phys. Rev. Lett. **113**, 047203 (2014).
[11] S. Emori, E. Martinez, K.-J. Lee, H.-W. Lee, U. Bauer, S.-M. Ahn, P. Agrawal, D. C. Bono, and G. S. D. Beach, Phys. Rev. B **90**, 184427 (2014).
[12] I. Gross, L. J. Martínez, J.-P. Tetienne, T. Hingant, J.-F. Roch, K. Garcia, R. Soucaille, J. P. Adam, J.-V. Kim, S. Rohart, A. Thiaville, J. Torrejon, M. Hayashi, and V. Jacques, Phys. Rev. B **94**, 064413 (2016).
[13] F. Freimuth, S. Blügel, and Y. Mokrousov, J. Phys.: Condens. Matter **26**, 104202 (2014).
[14] B. Zimmermann, M. Heide, G. Bihlmayer, and S. Blügel, Phys. Rev. B **90**, 115427 (2014).
[15] C. Moreau-Luchaire, C. Moutafis, N. Reyren, J. Sampaio, C. A. F. Vaz, N. Van Horne, K. Bouzehouane, K. Garcia, C. Deranlot, P. Warnicke, P. Wohlhüter, J.-M. George, M. Weigand, J. Raabe, V. Cros, and A. Fert, Nat. Nanotechnol. **11**, 444 (2016).
[16] Y. P. Kabanov, Y. L. Iunin, V. I. Nikitenko, A. J. Shapiro, R. D. Shull, L. Y. Zhu, and C. L. Chien, IEEE Trans. Magn. **46**, 2220 (2010).
[17] A. Hrabec, N. A. Porter, A. Wells, M. J. Benitez, G. Burnell, S. McVitie, D. McGrouther, T. A. Moore, and C. H. Marrows, Phys. Rev. B **90**, 020402(R) (2014).
[18] H. Yang, A. Thiaville, S. Rohart, A. Fert, and M. Chshiev, Phys. Rev. Lett. **115**, 267210 (2015).
[19] G. Chen, T. Ma, A. T. N'Diaye, H. Kwon, C. Won, Y. Wu, and A. K. Schmid, Nat. Commun. **4**, 2671 (2013).
[20] N.-H. Kim, J. Jung, J. Cho, D.-S. Han, Y. Yin, J.-S. Kim, H. J. M. Swagten, and C.-Y. You, Appl. Phys. Lett. **108**, 142406 (2016).
[21] J. Cho, N.-H. Kim, S. K. Kang, H.-K. Hwang, J. Jung, H. J. M. Swagten, J.-S. Kim, and C.-Y. You, J. Phys. D **50**, 425004 (2017).
[22] K. Inomata, N. Ikeda, N. Tezuka, R. Goto, S. Sugimoto, M. Wojcik, and E. Jedryka, Sci. Technol. Adv. Mater. **9**, 014101 (2008).
[23] M. Belmeguenai, H. Tuzcuoglu, M. S. Gabor, T. Petrisor, Jr., C. Tiusan, D. Berling, F. Zighem, T. Chauveau, S. M. Chérif, and P. Moch, Phys. Rev. B **87**, 184431 (2013).
[24] V. L. Zhang, K. Di, H. S. Lim, S. C. Ng, M. H. Kuok, J. Yu, J. Yoon, X. Qiu, and H. Yang, Appl. Phys. Lett. **107**, 022402 (2015).
[25] M. Kostylev, J. Appl. Phys. **115**, 233902 (2014).
[26] K. Di, V. L. Zhang, H. S. Lim, S. C. Ng, M. H. Kuok, J. Yu, J. Yoon, X. Qiu, and H. Yang, Phys. Rev. Lett. **114**, 047201 (2015).
[27] M. Belmeguenai, M. S. Gabor, F. Zighem, Y. Roussigné, D. Faurie, and C. Tiusan, Phys. Rev. B **94**, 104424 (2016).
[28] K.-S. Ryu, S.-H. Yang, L. Thomas, and S. S. P. Parkin, Nat. Commun. **5**, 3910 (2014).
[29] M. Belmeguenai, H. Tuzcuoglu, M. Gabor, T. Petrisor, Jr., C. Tiusan, F. Zighem, S. M. Chérif, and P. Moch, J. Appl. Phys. **115**, 043918 (2014).
[30] M. T. Johnson, P. J. H. Bloemenz, F. J. A. den Broeder, and J. J. de Vries, Rep. Prog. Phys. **59**, 1409 (1996).

[31] F. J. A. den Broeder, W. Hoving, and P. J. H. Bloemen, J. Magn. Magn. Mater. **93**, 562 (1991).
[32] C. A. F. Vaz, J. A. C. Bland, and G. Lauhoff, Rep. Prog. Phys. **71**, 056501 (2008).
[33] M. Gueye, B. M. Wague, F. Zighem, M. Belmeguenai, M. S. Gabor, T. Petrisor, Jr., C. Tiusan, S. Mercone, and D. Faurie, Appl. Phys. Lett. **105**, 062409 (2014).
[34] H. Szymczak, M. Rewiefiski, and R. Zuberek, J. Magn. Magn. Mater. **139**, 151 (1995).
[35] M. Belmeguenai, M. S. Gabor, Y. Roussigné, A. Stashkevich, S. M. Chérif, F. Zighem, and C. Tiusan, Phys. Rev. B **93**, 174407 (2016).
[36] J. Cho, N.-H. Kim, S. Lee, J.-S. Kim, R. Lavrijsen, A. Solignac, Y. Yin, D.-S. Han, N. J. J. van Hoof, H. J. M. Swagten, B. Koopmans, and Ch.-Y. You, Nat. Commun. **6**, 7635 (2015).
[37] A. Fert and P. M. Levy, Phys. Rev. Lett. **44**, 1538 (1980).
[38] H. T. Nembach, J. M. Shaw, M. Weiler, E. Jué, and T. J. Silva, Nat. Phys. **11**, 825 (2015).